INSTITUT DE FRANCE
Académie des sciences

Comptes Rendus
Mécanique

Hajer Boussetta, Abdelouahed Laksimi, Hocine Kebir, Moez Beyaoui, Lassaad Walha and Mohamed Haddar

Plastic-damage-response analysis of glass/polyester filament wound structures: 3D meso-scale numerical modelling, experimental identification and validation

Volume 348, issue 5 (2020), p. 315-333

https://doi.org/10.5802/crmeca.10

Les Comptes Rendus. Mécanique *sont membres du*
Centre Mersenne pour l'édition scientifique ouverte
www.centre-mersenne.org
e-ISSN : 1873-7234

Comptes Rendus
Mécanique
2020, 348, nº 5, p. 315-333
`https://doi.org/10.5802/crmeca.10`

Plastic-damage-response analysis of glass/polyester filament wound structures: 3D meso-scale numerical modelling, experimental identification and validation

Hajer Boussetta[*, a, b], **Abdelouahed Laksimi**[b], **Hocine Kebir**[b], **Moez Beyaoui**[a], **Lassaad Walha**[a] and **Mohamed Haddar**[a]

[a] University of Sfax, LA2MP, ENIS, Route Soukra km 3.5, 3038 Sfax, Tunisia

[b] Technology University of Compiègne, Laboratoire Roberval UMR 6253, 60205 Compiègne cedex, France

E-mails: hajer.boussetta91@gmail.com (H. Boussetta), abdelouahed.laksimi@utc.fr (A. Laksimi), hocine.kebir@utc.fr (H. Kebir), moez.beyaoui@yahoo.fr (M. Beyaoui), walhalassaad@yahoo.fr (L. Walha), mohamed.haddar@enis.rnu.tn (M. Haddar)

Abstract. The aim of this paper is to propose a theoretical meso-model describing the nonlinear behaviour of filament wound glass–polyester composite structures based on a progressive damage and failure analysis. This model has been implemented in the finite element modelling software Abaqus through the user material subroutine and then validated by experimental investigations. Numerical results have been compared with experimental data obtained from a set of tests on representative specimens using the strain measurement technique.

Keywords. Filament wound composite, Finite element modelling, Experimental validation, Progressive damage and failure analysis, Meso-model, Nonlinear behaviour.

Manuscript received 4th December 2019, accepted 16th March 2020.

1. Introduction

Glass reinforced plastic pipes are highly competitive in fluid transport applications owing to their good mechanical and chemical properties with the added advantage of lightness compared to other conventional materials [1–3].

Prior to designing or optimizing such structures, numerical modelling is usually required to test their load-bearing capacity without resorting to experimental tests that could involve huge costs in terms of time, money and effort. In addition, this method is useful for identifying the mechanical properties of pipes with the same material constituents rather than expending effort in experimental characterization.

---

[*] Corresponding author.

Nevertheless, modelling these structures has always remained an important aim from the engineering point of view because of their various complex damage mechanisms, which are hard to predict numerically, especially when subjected to biaxial loadings such as internal and external hydrostatic pressure. In fact, although researchers have become increasingly interested in the modelling of filament wound composite structures, most of their studies have been limited on the use of failure criteria [4–8] by referring to mathematical equations in stress or strain space to separate "failed" from "unfailed" states. In these equations, the damage initiation and evolution have not been taken into account, and different damage phenomena have been overlooked. However, the prediction of the load-bearing capacity of composite cylindrical structures functioning under complex loadings consists certainly in the investigation of their stiffness degradation, which should involve the damage initiation and evolution phenomenon [9]. Therefore, "continuous damage mechanics" is an alternative approach, which consists in the modelling of damage mechanism effects on material stiffness degradation using state variables. Various research studies aimed at numerical modelling as well as the optimal design of composite pressure vessels have been collected in the review by Liu *et al.* [10]. In fact, failure in filament wound composite structures has been well emphasized. However, modelling that deals with progressive damage has not been deeply studied. In addition, different failure phenomena are not always taken into account, in particular, the delamination between plies, which is often overlooked. Moreover, the composite is considered as a shell laminate. Therefore, attempts to develop the most complete and efficient numerical model of these structures continue to be the object of our study.

To achieve this aim, an experimental characterization study is essential, which was the purpose of my previous work [11]. Experimental monitoring by acoustic emission of different damage phenomena occurring in the loaded material was carried out. Based on this experimental study, a mathematical formulation of the model describing the behaviour of the material has been developed. The mesoscopic scale has been adopted. This choice was based on experimental observations showing two scales of initiation and evolution of degradation, which are the ply where the matrix cracks, the fibres break as well as the decohesions between fibres and the matrix arise and develop; and the interface where the delaminations are located. These delaminations have been modelled on the basis of fracture mechanics by the development of a cohesive zone model.

During the development of the ply model, a set of parameters is involved whose identification has required the use of special experimental devices. A numerical tool has been also deployed to identify the interface model parameters. As the reliability of the numerical model depends strongly on the extent of accuracy of its parameters, great attention has been given to this phase of study.

The analytical ply model has been implemented in Abaqus by the finite element method via the user material (UMAT) subroutine.

The simulation of the interface behaviour has been performed directly on the CAE interface of the software. In parallel with the development of the whole model, a set of experimental tensile tests has been carried out on representative specimens to validate the reliability of the numerical model.

2. Materials and specimens

The glass fibre used is E6-CR type, Direct Roving 386; it is compatible with polyester resin. Providing this type of reinforcement to the polyester resin leads to a composite material that is widely used and is a common component in the manufacture of pipes and pressure vessels, as well as chemical storage tanks, thanks to its good physical and chemical mechanical properties.

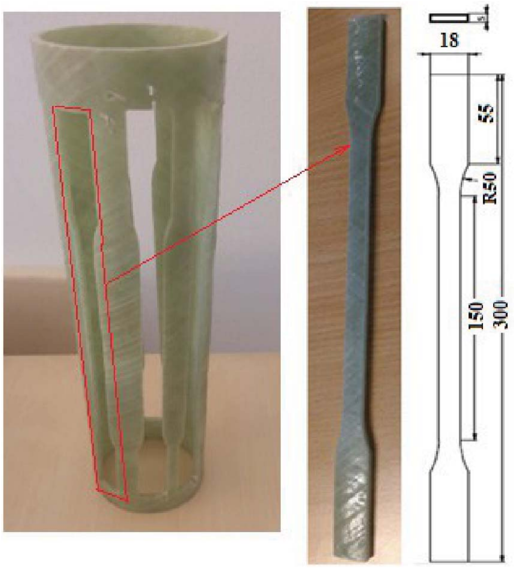

Figure 1. Longitudinal test specimen.

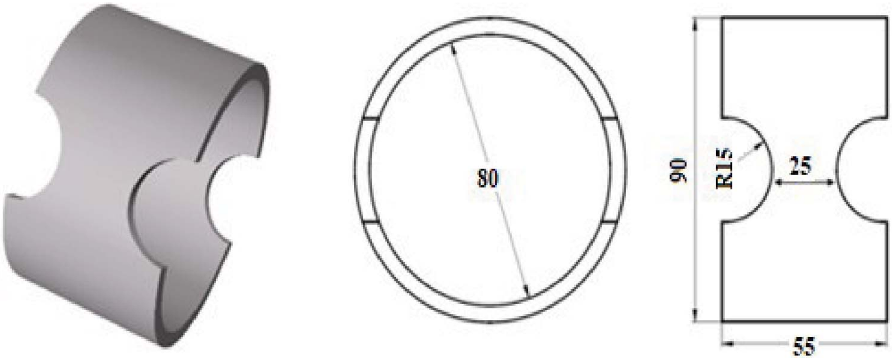

Figure 2. Cylindrical test specimen.

Regarding the resin, it is an unsaturated polyester of type PolyPol-1023, which is a medium-viscosity resin with excellent resilience.

The specimens were manufactured by filament winding. First, a tube is obtained by winding a mandrel with the required draping. The tube is then cut along the longitudinal axis (Figure 1) according to the standard ISO 8513:2016 [12] to obtain filament wound test specimens having a small curvature.

Cylindrical specimens (rings) obtained according to the standard ASTM D2290 [13] were also used in this study (Figure 2).

All the results of this study are based on monotonic tensile and compressive testing performed using an Instron machine, whose grips were moved at a constant speed of 1 mm/min.

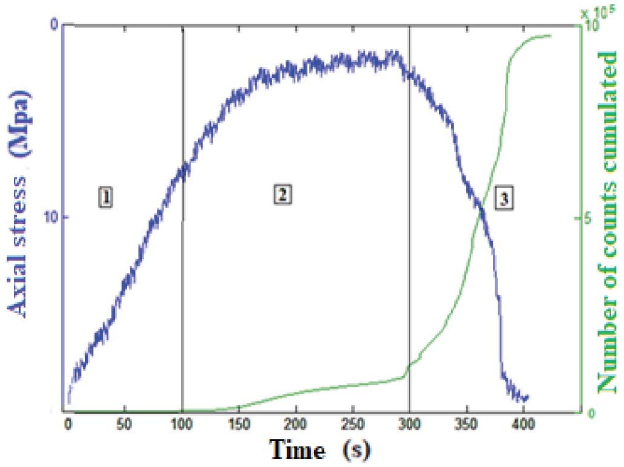

Figure 3. Correlation between the evolution of acoustic activity and the behaviour law [11].

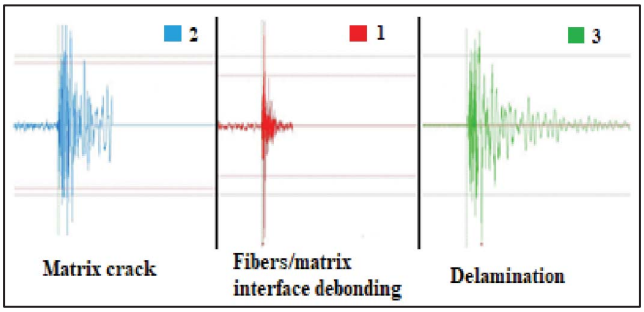

Figure 4. Distinction among the signal waveforms according to each damage mechanism [11].

3. Overview of material behaviour

In a previous work [11], the behaviour of the material under study was deeply characterized through an acoustic emission investigation. Relevant tensile tests, together with in situ acoustic emission monitoring, were conducted on ±55° longitudinal test specimens.

The evolution of acoustic activity has been correlated to the axial loads as a function of the apparent deformation within the specimen (Figure 3). Therefore, it is possible to deduce that the total life of the material under study is divided into three phases:

- Phase 1: The material is linear elastic, where it does not undergo any damage or plasticity.
- Phase 2: The curve begins to lose its linearity slightly because micro-cracking of the resin begins.
- Phase 3: The material is subjected to significant damage followed by its total ruin.

Then, an unsupervised pattern recognition analysis was conducted on the acoustic emission signals to distinguish the different types of damage that can occur in this kind of material being constrained (Figure 4).

Based on these experimental observations, the numerical model describing the material behaviour has been developed.

The progressive damage noticed experimentally has been considered. In addition, the different failure phenomena observed have been considered through the involvement of internal state variables, related to stiffness degradation, in the constitutive law.

4. Numerical modelling

4.1. *Ply model*

4.1.1. *Mathematical formulation*

By relying on continuous damage mechanisms, Barbero [14] developed a damage model for composite laminates. Based on this model, the behaviour of each ply of the material under study has been simulated.

According to the experimental knowledge acquired about ply degradation, three damage variables d1, d2 and d3 are defined and associated with the stiffness decrease in each direction of the material.

The concept of effective stress introduced by Kasanov [15] and Rabotnov [16] has been adopted. This concept implies that it is convenient to write the constitutive law for a damaged material by introducing effective stress $\overline{\sigma}$ instead of nominal stress σ.

The mathematical formulation of the model is based on the irreversible thermodynamic process according to the irreversible behaviour of plasticity coupled with damage progression. A set of internal variables is then used to define the state of the material throughout time. Therefore, the Helmholtz free energy $\psi = \psi(\varepsilon, \varepsilon^p, D, p, \delta)$ is postulated to describe the dissipative phenomenon involved and record the history of the solid.

Table 2 lists the state internal variables describing each mechanism as well as its corresponding thermodynamic forces derived from the Helmholtz free energy.

✔ The activation of the plastic dissipation phenomenon is governed by the yield surface $g^p = 0$, which is a function of thermodynamic potentials (σ, R) in the effective configuration associated with the internal state variables ε and p, respectively:

$$g^p = g^p(\sigma) - R(p) - R_0 = (f_{ij}\overline{\sigma}_i\overline{\sigma}_j + f_i\overline{\sigma}_i - R(p) - R_0)^{\frac{1}{2}} = 0. \tag{1}$$

This formulation is deduced from the Tsai–Wu criterion [17]. Here, f_{ij} and f_i are coefficients of the yield surface depending on the effective stresses at break $\overline{F_i}$ $(i = 1, 2 \ldots 6)$, p is the hardening variable, R_0 is the initial unrecoverable-strain threshold and $R(p)$ is the hardening function.

✔ The energy dissipation caused by damage progression is governed by the surface $g^d = 0$, a function of thermodynamic potentials Y and γ associated with the internal state variables D and δ, respectively. This surface delimits a region in the space of thermodynamic forces Y, where damage does not occur:

$$g^d(Y(D), \gamma(\delta)) = \sqrt{Y^N J Y^N} + \sqrt{Y^S H Y^S} - (\gamma(\delta) + \gamma_0) = 0. \tag{2}$$

Here, D is the second-order damage tensor, δ is a hardening variable, γ_0 is the initial damage threshold, J and H are two diagonal tensors controlling the shape of the damage surface whose terms (J_1, J_2, J_3) and (H_1, H_2, H_3), respectively, can be determined based on the elastic properties and the ultimate strengths estimated from uniaxial loading tests.

✔ Another consistency condition must be proven to admit the existence of both damage progression and plasticity: $(dg^d = 0)$ and $(dg^p = 0)$, respectively.

To solve the nonlinear finite element problem, it is necessary to integrate the constitutive equation governing the material behaviour. Thus, the tangent constitutive equation is presented. It is given by

$$\dot{\sigma} = C^{\mathrm{epd}} : \dot{\varepsilon}, \tag{3}$$

Table 1. Ply model parameters

Properties	Values
E_{11} (Gpa): Longitudinal modulus of the virgin material	55.3
E_{11}^{*} (Gpa): Longitudinal modulus of the damaged material	55.3
E_{22} (Gpa): Transverse modulus of the virgin material	11.23
E_{22}^{*} (Gpa): Transverse modulus of the damaged material	10.5
G_{12} (Gpa): In-plane shear modulus of the virgin material	4.5
G_{12}^{*} (Gpa): In-plane shear modulus of the damaged material	1.87
E_{33} (Gpa): Out-of-plane transverse elasticity	11.23
G_{13} (Gpa): Out-of-plane axial shear modulus	4.58
G_{23} (Gpa): Transverse shear modulus	3.25
υ_{12}: In-plane axial Poisson's ratio	0.322
υ_{21}: In-plane transverse Poisson's ratio	0.051
υ_{13}: Out-of-plane axial Poisson's ratio	0.306
υ_{23}: Transverse Poisson's ratio	0.66
F_{t11} (Mpa): Longitudinal tensile strength	505
F_{t22} (Mpa): Transverse tensile strength	18
F_{t6} (Mpa): In-plane shear strength	34
F_{c11} (Mpa): Longitudinal compressive strength	388
F_{c22} (Mpa): Transverse compressive strength	18

Table 2. State variables and its corresponding thermodynamic forces

Mechanism	State variable	Thermodynamic force	
Elasticity	ε	$\sigma = C(D)(\varepsilon - \varepsilon^{p})$	(1)
Plasticity	ε^{p}	$\sigma = C(D)(\varepsilon - \varepsilon^{p})$	(2)
Yield hardening	p	$R = c_1^{p}\left(\exp\left(\frac{p}{c_2^{p}}\right) - 1\right)$	(3)
Damage	D	$Y = -\frac{1}{2}(\varepsilon - \varepsilon_{p})\frac{\mathrm{d}C}{\mathrm{d}D}(\varepsilon - \varepsilon^{p})$	(4)
Damage hardening	δ	$\gamma = c_1^{d}\left(\exp\left(\frac{\delta}{c_2^{d}}\right) - 1\right)\gamma(\delta)$	(5)

$C(D)$ is the damage stiffness tensor; c_1^{p}, c_1^{d} and c_2^{d} are the material parameters.

where C^{epd} is the damage tangent constitutive tensor, which depends on the strain tensor evolution and the material state.

4.1.2. *Identification of parameters*

The theoretical model developed in the previous section includes a set of parameters listed in Tables 1 and 3. These parameters depend on specific material properties whose identification has been carried out experimentally by following the approach described below.

✔ *Normal coefficients of the damage surface*

The coefficients J_1, J_2 and J_3 represent the damage effect caused by axial loading on the shape of the damage surface. Therefore, they are related to the mechanical properties obtained by tensile testing conducted in the material directions, which are the elasticity moduli E_1, E_2 and

E_3; Poisson's ratios ϑ_{12}, ϑ_{23} and ϑ_{13}; and the ultimate tensile and compressive strengths F_{1t}, F_{1c}, F_{2t}, F_{2c}, F_{3t} and F_{3c}.

- J_1 represents the fibre breaking effect on the damage surface during longitudinal loading. To determine this coefficient, the case of longitudinal uniaxial loading is considered: $(\sigma_1 \neq 0, \sigma_2 = 0, \sigma_3 = 0, \sigma_4 = 0, \sigma_5 = 0, \sigma_6 = 0)$.
  $g^d = 0$ is written as follows:
  $$F_{t1}^2 \frac{\overline{S}_{11}}{(1-d_1)^3} \sqrt{J_1} = \gamma^* + \gamma_0 = 1. \tag{4}$$
  Here, γ^* represents damage hardening at the imminent break; $1 - d_1 = C_{11}^* / \overline{C_{11}}$; $\overline{C}_{11}$ and C_{11}^* are the longitudinal stiffness moduli of the material in the virgin and damaged states, respectively.
- J_2 denotes the effect of matrix failure on the damage surface throughout transverse loading. To determine this coefficient, we consider the case of transverse uniaxial loading: $(\sigma_2 \neq 0, \sigma_1 = 0, \sigma_3 = 0, \sigma_4 = 0, \sigma_5 = 0, \sigma_6 = 0)$.
  $g^d = 0$ is written as follows:
  $$F_{2t}^2 \frac{\overline{S}_{22}}{(1-d_2)^3} \sqrt{J_2} = \gamma^* + \gamma_0 = 1. \tag{5}$$
  Here, $1 - d_2 = C_{22}^* / \overline{C_{22}}$; $\overline{C}_{22}$ and C_{22}^* are the transverse stiffness moduli of the material in the virgin and damaged states, respectively.
- J_3 is assumed equal to J_2 since it also denotes the effect of matrix failure on the damage surface.

✔ *Shear coefficients of the damage surface*

The coefficients H_1, H_2 and H_3 represent the effect of the damage caused by the shear loads on the shape of the damage surface g^d. Therefore, they are related to the mechanical properties obtained by shear tests. These are the in-plane and out-of-plane shear moduli of the material in the virgin state (G_{12}, G_{13}) and the damaged state just before the break (G_{12}^*, G_{13}^*). The ultimate shear strengths in the plane and out of the plane (F_6, F_5) are also required.

- H_1 represents the fibre breaking effect on the damage surface during shear loading. Nevertheless, according to the experiments, during pure shear loading, the damage in the direction of the fibres is negligible ($d_1 = 0$); so we estimate that $H_1 = 0$.
- H_2 and H_3 characterize the matrix degradation effect on the damage surface during shear loading; therefore, they are assumed to be equal.

The in-plane shear loading is considered: $(\sigma_6 \neq 0, \sigma_1 = 0, \sigma_2 = 0, \sigma_3 = 0, \sigma_4 = 0, \sigma_5 = 0)$.
At the imminent break, $g^d = 0$ is written as follows:

$$F_6^2 \frac{2\overline{S}_{66}}{(1-d_2)^3} \sqrt{H_2} = \gamma^* + \gamma_0 = 1. \tag{6}$$

Here, $1 - d_2 = G_{12}^* / \overline{G_{12}}$; F_6, $\overline{S}_{66}$, G_{12}^* and $\overline{G}_{12}$ are determined from the stress versus strain curve of a shear test obtained by carrying out a tensile test on a longitudinal specimen whose fibre direction is ±45° while assuming that

$$2\varepsilon_{12} = \varepsilon_{xx} - \varepsilon_{yy}, \tag{7}$$

$$\sigma_{12} = \frac{\sigma_{xx}}{2}, \tag{8}$$

where σ_{xx} and ε_{xx} are the stress and the strain measured in the loading direction, and ε_{yy} represents the strain measured in the transverse direction.

✔ *Coefficients of the yield surface*

The coefficients $f_1, f_2, f_3, f_{12}, f_{13}, f_{23}, f_{11}, f_{66}$ and f_{22} are directly related to the effective strengths $\overline{F_i}$ obtained from uniaxial tensile and compressive tests.

$$f_1 = \frac{1}{\overline{F}_{1t}} - \frac{1}{\overline{F}_{1c}}; \quad f_2 = \frac{1}{\overline{F}_{2t}} - \frac{1}{\overline{F}_{2c}}; \quad f_3 = \frac{1}{\overline{F}_{3t}} - \frac{1}{\overline{F}_{3c}} \tag{9}$$

$$f_{11} = \frac{1}{\overline{F}_{1t}\overline{F}_{1c}}; \quad f_{22} = \frac{1}{\overline{F}_{2t}\overline{F}_{2c}}; \quad f_{66} = \frac{1}{\overline{F}_6{}^2} \tag{10}$$

$$f_{12} \cong -0.5\sqrt{f_{11}f_{22}}; \quad f_{13} \cong -0.5\sqrt{f_{11}f_{33}}; \quad f_{23} \cong -0.5\sqrt{f_{33}f_{22}}. \tag{11}$$

✔ *Hardening coefficients*

- δ and p:

As this is a case of in-plane shear stress, g^d and g^p are written as follows:

$$g^d = \sqrt{H_2}Y_{22}^s - (\gamma(\delta) + \gamma_0) = \sqrt{H_2}\sigma_6^2 \frac{2\overline{S}_{66}}{(1-d_2)^2} - c_1^d\left(\exp\left(\frac{\delta}{c_2^d}\right) - 1\right) - \gamma_0, \tag{12}$$

$$g^p = \frac{\overline{\sigma}_6}{\overline{F}_6} - (R(p) + R_0) = \frac{\overline{\sigma}_6}{\overline{F}_6} - c_1^p\left(\exp\left(\frac{p}{c_2^p}\right) - 1\right) - R_0. \tag{13}$$

The evolution of the damage variable as well as that of the associated hardening variable is governed by the kinetic equations

$$\dot{D} = \dot{\lambda}^d \frac{\mathrm{d}g^d}{\mathrm{d}Y}, \tag{14}$$

$$\dot{\delta} = \dot{\lambda}^d \frac{\mathrm{d}g^d}{\mathrm{d}\gamma}. \tag{15}$$

Furthermore, for plasticity, the evolution of the variables relating to this phenomenon is governed by the following kinetic equations:

$$\dot{\overline{\varepsilon}}^p = \dot{\lambda}^p \frac{\mathrm{d}g^p}{\mathrm{d}\overline{\sigma}}, \tag{16}$$

$$\dot{p} = \dot{\lambda}^p \frac{\mathrm{d}g^p}{\mathrm{d}R}. \tag{17}$$

Based on the preceding equations, we obtain

$$\frac{\dot{D}}{\dot{\delta}} = \frac{\dot{\lambda}^d \frac{\mathrm{d}g^d}{\mathrm{d}Y}}{\dot{\lambda}^d \frac{\mathrm{d}g^d}{\mathrm{d}\gamma}} = -\sqrt{H_2}, \tag{18}$$

$$\frac{\dot{\overline{\varepsilon}}^p}{\dot{p}} = \frac{\dot{\lambda}^p \frac{\mathrm{d}g^p}{\mathrm{d}\overline{\sigma}}}{\dot{\lambda}^p \frac{\mathrm{d}g^p}{\mathrm{d}R}} = -\frac{1}{\overline{F}_6}, \tag{19}$$

where $\dot{\lambda}^p$ and $\dot{\lambda}^d$ are the plastic and damage multipliers, respectively.

Therefore, the integration of g^d and g^p with initial conditions for in-plane shear stress allows us to write the hardening variables p and δ as functions of other observable measurable variables $\overline{\varepsilon}_6^p$ and d_2:

$$\delta = -\frac{1}{\sqrt{H_2}} d_2, \tag{20}$$

$$p = -\overline{F}_6\overline{\varepsilon}_6{}^p. \tag{21}$$

- R_0 and γ_0:

To identify R_0 and γ_0, it is necessary to determine experimentally the yield stress F_6^p, which is the highest shear stress without significant plastic strain, and the initial damage threshold F_6^d, which is the highest shear stress without significant damage.

As it is under in-plane shear loading lower than the threshold value F_6^d, the material is considered undamaged ($d_2 = 0; \delta = 0$) and γ_0 can be deduced from the damage surface expression g^d: $\gamma_0 = \sqrt{H_2} 2\overline{S}_{66}(F_6^d)^2$.

Similarly, when the material is subjected to pure shear loading approaching the threshold F_6^p, the plasticity is considered absent ($\overline{\varepsilon}_6^p = 0; p = 0$) and R_0 can be deduced from the yield surface expression g^p:

$$R_0 = \frac{\overline{F}_6^P}{\overline{F}_6}. \tag{22}$$

- c_1^d, c_2^d and c_1^p, c_2^p:

To identify c_1^d, c_2^d and c_1^p, c_2^p, the stress–strain response of a typical in-plane shear test with several loading–unloading cycles was used.

By integrating the expression of δ (25) into the expression $g^d = 0$ (17), we obtain the expression of the shear stress σ_6 as a function of the damage variable d_2:

$$\sigma_6 = c_1^d \left(\exp\left(-\frac{d_2}{\sqrt{H_2} c_2^d}\right) - 1\right)\left(\frac{(1-d_2)^2}{2\overline{S_{66}}\sqrt{H_2}}\right) + (F_6^d)^2. \tag{23}$$

Given H_2 and $\overline{S_{66}}$, we are able to determine c_1^d and c_2^d using the curve represented by $\sigma_6 = f(\sqrt{1-d_2})$ (Figure 11).

Likewise, by integrating the expression of p into the expression $g^p = 0$ (18), the expression of the effective shear stress $\overline{\sigma_6}$ can be obtained as a function of the effective plastic strain $\overline{\varepsilon}_6^p$:

$$\overline{\sigma_6} = \overline{F}_6^P \left(c_1^p \left(\exp\left(\frac{-\overline{F}_6^P \overline{\varepsilon}_6{}^p}{c_2^p}\right) - 1\right) + R_0\right). \tag{24}$$

Given $\overline{F}_6^P$ and R_0, c_1^p and c_2^p can be determined using the measurable values of $\overline{\sigma_6}$ versus $\overline{\varepsilon}_6{}^p$ (Figure 10) obtained from the cyclic shear test.

Results:

✔ *Properties in the longitudinal direction*

The determination of longitudinal properties has necessitated tensile and compressive loadings on 0° longitudinal specimens. However, obtaining these specimens requires a special device (flat specimens formed by filament winding around a flat-faced mandrel). Indeed, winding fibres around a cylindrical mandrel within a degree of 0° is impossible. Thus, the test has been conducted on ±90° cylindrical specimens.

The experimental devices used to perform tensile and compressive tests on cylindrical specimens are presented in Figures 5 and 6.

The stress–strain response results of each test are also illustrated throughout these figures. The measured circumferential stress is equal to half of the applied load F divided by the area of the section ($A = 25$ mm) where the gauge is located: $\sigma = F/2A$.

To determine Poisson's ratio, the measurement of the strain in both directions 1 and 2 is required.

✔ *Properties in the transverse direction*

In-plane transverse properties have been obtained by testing ±90° longitudinal specimens in tension and compression. In-plane and out-of-plane transverse properties are considered to be equal: $E_3 = E_2$, $F_{3t} = F_{2t}$ and $F_{3c} = F_{2c}$.

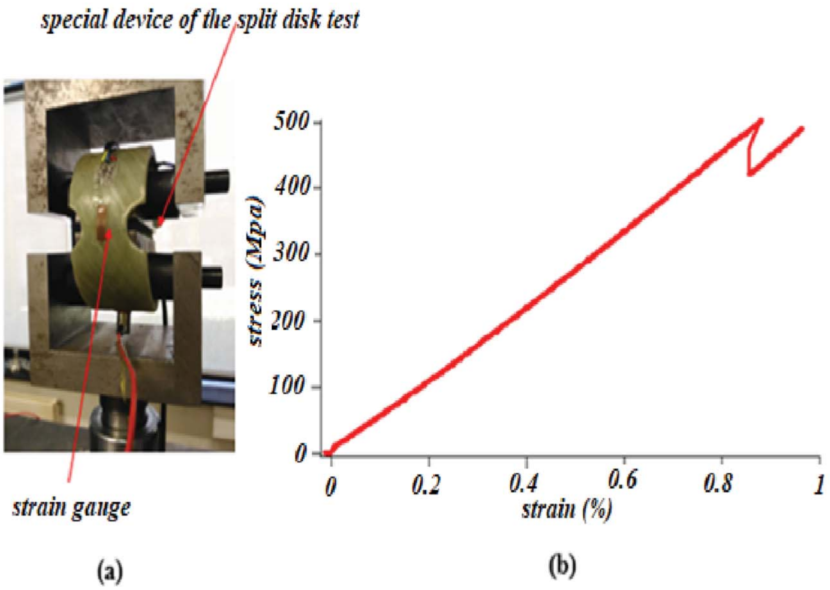

Figure 5. ±90° cylindrical specimen under tensile test: (a) set-up; (b) response.

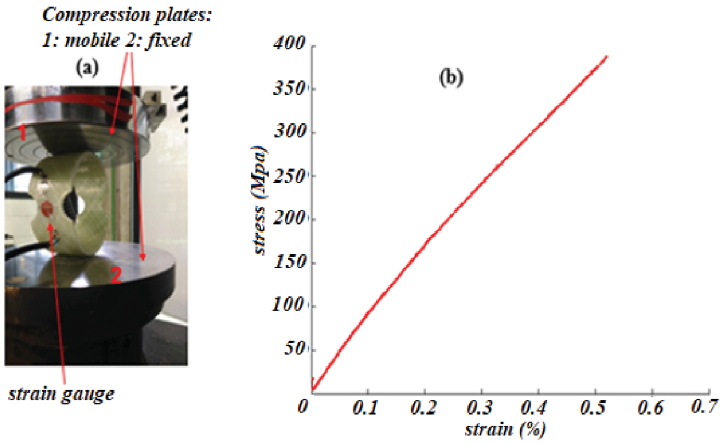

Figure 6. (a) Rings under compressive test; (b) compressive test response of 90° ring.

The experimental set-up used to perform tensile and compressive tests on longitudinal specimens is presented in Figures 7 and 8. The stress–strain responses of these tests are well illustrated.

✔ *In-plane shear properties*

In addition to the shear modulus G_{12} and the ultimate stress F_6, other properties involved in the damage model developed in the previous section are determined.

These properties are related to the stiffness reduction of the material, which is a result of its failure, as well as to work hardening, which is a consequence of plastic deformation. Therefore, a cyclic loading test (Figure 9) has been performed on ±45° longitudinal specimens to enable the investigation of these two phenomena after each cycle. Indeed, by measuring the in-plane shear stress σ_6, the plastic in-plane shear strain ε_6 and the integrity variable $\Omega_{12} = \sqrt{1-d_2}$ at different

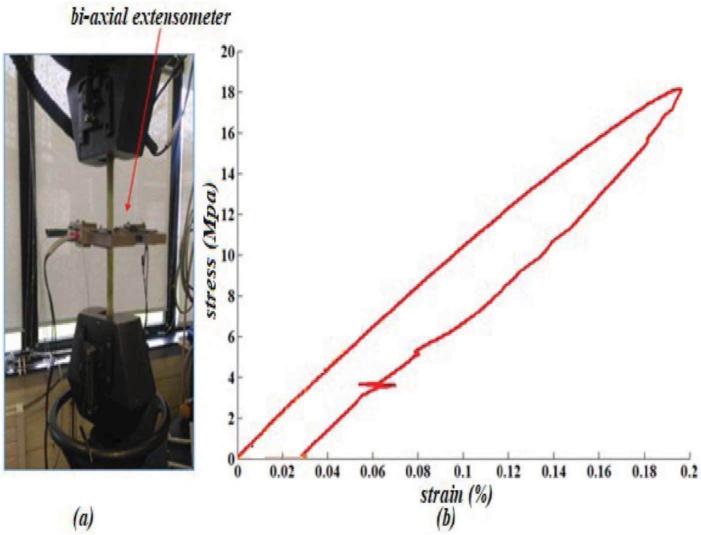

Figure 7. ±90° longitudinal specimen under tensile test: (a) set-up; (b) response.

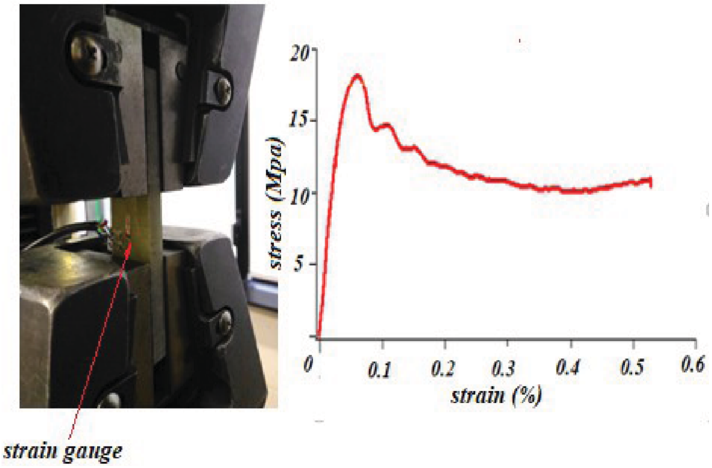

Figure 8. ±90° longitudinal specimen under compressive test: (a) set-up; (b) response.

points and by following the approach detailed above, the parameters $(c_1^d; c_2^d; \gamma_0; c_1^p; c_2^p; R_0)$ can be identified.

✔ *Transverse shear properties*

The measurement of shear properties in composites is a challenging task [18]. Indeed, it is very difficult to measure the transverse shear modulus G_{23} and its corresponding shear strength as well as the transverse Poisson's ratio ϑ_{23}. Thus, the theoretical approach "rule of mixtures" has been used to identify these properties based on the composite constituents' mechanical properties specified by the manufacturer.

All results measured experimentally or calculated theoretically above are illustrated in Tables 1, 4 and 5.

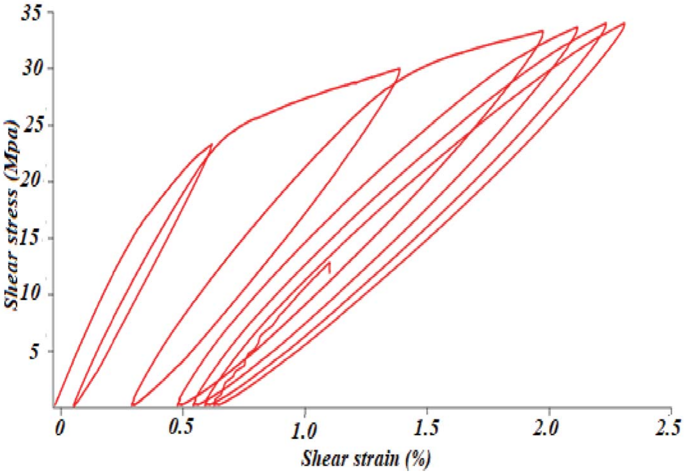

Figure 9. Response of cyclic tensile test on ±45° longitudinal specimen.

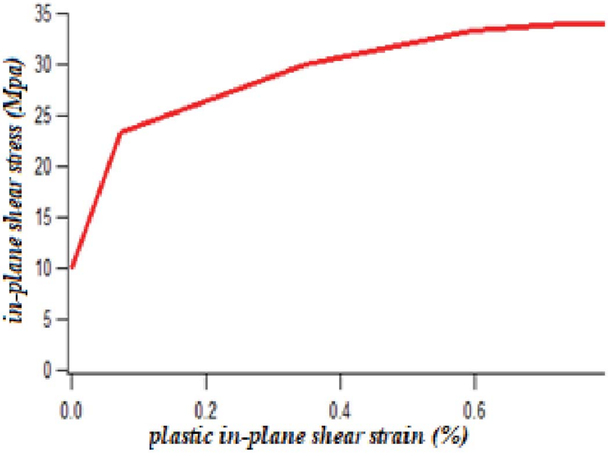

Figure 10. In-plane shear stress $\overline{\sigma_6}$ (Mpa) versus plastic in-plane shear strain $\overline{\varepsilon}_6^p$ (%).

Table 3. Specific mechanical properties of the material

Shear damage constitutive vectors	H_1, H_2, H_3
Normal damage constitutive vectors	J_1, J_2 ,J_3
Damage hardening coefficients	c_1^d, c_2^d, γ_0
Yield hardening coefficients	c_1^p, R_0
Coefficients of the yield surface	f_i, f_{ij} $(i = 1,2\ldots6)$

4.2. *Interface model*

4.2.1. *Mathematical formulation*

Based on the principles of fracture mechanics, several numerical tools can be used to model delamination in composite structures [19]. The most widely used are those including the "virtual

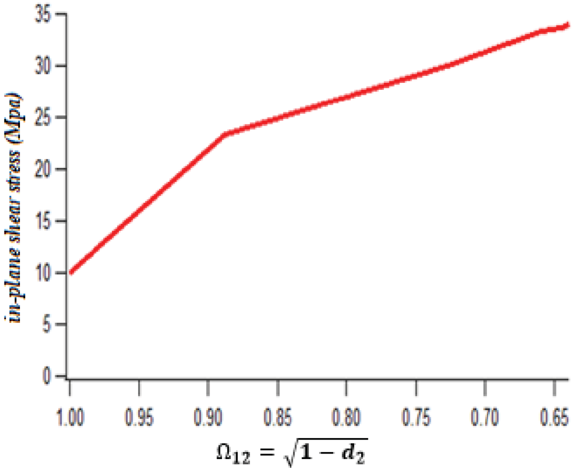

Figure 11. In-plane shear stress σ_6 (Mpa) versus integrity variable $\Omega_{12} = \sqrt{1-d_2}$.

Table 4. Values of specific mechanical properties of the material

Shear damage constitutive vectors	$H_1 = 0$, $H_2 = H_3 = 0.113$
Normal damage constitutive vectors	$J_1 = 3.4 \times 10^{-3}$, $J_2 = J_3 = 0.301$
Damage hardening coefficients	$c_1^d = 0.024, c_2^d = -0.48,$ $\gamma_0 = 14.41 \times 10^{-3}$
Yield hardening coefficients	$c_1^p = -0.568, c_2^p = 0.075$, $R_0 = 0.187$

Table 5. Release energy rates and stress intensity factor values

K_{IC} (Mpa $\sqrt{m}$)	7.57
K_{IIC} (Mpa $\sqrt{m}$)	1.18
K_{IIIC} (Mpa $\sqrt{m}$)	0.31
G_{IC} (kJ/m^2)	4.95
G_{IIC} (kJ/m^2)	0.12
G_{IIIC} (kJ/m^2)	0.012
η	1.45

crack closure technique” (VCCT) or the “cohesive zone models”. However, the use of cohesive zone models is more reliable because of their ability to take into account both the “initiation” and the “progression” of failure.

As a result, the “cohesive zone models” is the technique used in this study to model the interface.

This technique includes interface elements that lead to the opening of a crack according to a cohesive law based on the use of either the internal damage variable notion or the traction/separation notion.

The cohesive traction/separation law, which is available in Abaqus/standard, has been used in the present study.

This law hypothesizes that at the point of any crack, cohesive forces appear and evolve in parallel with the progression of crack opening [20].

Various forms define this law in the literature: trapezoidal, exponential and polynomial. However, regardless of the form chosen, two parameters are usually included for different failure modes (modes 1–3), which are the energy release rate G^C and the maximum cohesive force σ^C.

This kind of law initially adopts a linear elastic behaviour followed by the initiation and the evolution of the damage. The elastic behaviour is written in terms of the constitutive matrix K, which links the normal and shear stresses to the normal and shear strains, respectively, over the entire interface:

$$t = \begin{Bmatrix} \sigma_n \\ \sigma_s \\ \sigma_t \end{Bmatrix} = \begin{bmatrix} k_{nn} & k_{ns} & k_{nt} \\ k_{ns} & k_{ss} & k_{st} \\ k_{nt} & k_{st} & k_{tt} \end{bmatrix} = \begin{Bmatrix} \delta_n \\ \delta_s \\ \delta_t \end{Bmatrix} = K\delta, \tag{25}$$

where σ_n is the normal stress; σ_s and σ_t are the shear stresses; δ_n, δ_s and δ_t are the corresponding separations.

Therefore, interface modelling by the method of cohesive zone models goes through three steps: the definition of the *elastic behaviour* of the interface throughout the identification of the constitutive matrix K; the definition of the *damage initiation criterion*; and then the definition of the *damage evolution law*.

✔ *Damage initiation criterion*

The damage initiation represents the initial crack at a point of cohesive contact. This phenomenon occurs when stresses and/or displacements obey one of these criteria: maximum or quadratic stress criterion and maximum or quadratic separation criterion [21].

The criterion used in this study is the quadratic stress criterion defined as

$$\left\{\frac{\sigma_n}{{\sigma_n}^0}\right\}^2 + \left\{\frac{\sigma_s}{{\sigma_s}^0}\right\}^2 + \left\{\frac{\sigma_t}{{\sigma_t}^0}\right\}^2 = 1. \tag{26}$$

✔ *Damage evolution law*

The fracture mechanics define three different modes of failure: the pure traction mode (mode 1), the pure shear mode (mode 2) and the pure torsion mode (mode 3). However, most real load cases are combinations of these three different modes. Thus, it is necessary to take into account the interaction between these modes in the modelling of the interface. Two types of criteria can be used on Abaqus to define the mixed mode of delamination: one based on tensile separations and the other based on energies [21].

In the present work, an energy criterion developed by Benzeggagh and Kenane [22] has been adopted. The damage progression is defined by the energy released when the crack propagates. In fact, it is considered that there is a break only if the energy release rate is greater than the cohesive energy G_T^C:

$$G_T^c = G_{\mathrm{I}}^c + \left((G_{\mathrm{II}}^c - G_{\mathrm{I}}^c)\frac{G_{\mathrm{II}}}{G_T} + (G_{\mathrm{III}}^c - G_{\mathrm{I}}^c)\frac{G_{\mathrm{III}}}{G_T}\right)\left(\frac{G_{\mathrm{II}} + G_{\mathrm{III}}}{G_T}\right)^{\eta}. \tag{27}$$

Critical energies G_{I}^c, G_{II}^c and G_{III}^c are characteristic parameters to be determined. η is also a parameter of the interface model called cohesive property, which could be determined from the previous equation by identifying G_{I}^c, G_{II}^c and G_{III}^c and G^C.

4.2.2. *Identification of parameters*

Energy release rates have been determined by using several experimental, analytical and numerical methods such as the VCCT (Irwin [8], Rybicki and Kanninen [9], Raju [10], Zou *et al.* [11], Krueger [14]), the method of the integral J (Rice [15]), the virtual crack extension technique (Hellen [16]) and the stiffness-derived method (Park [17]).

The integral J is the technique used to identify the parameters of the interface model defined above.

The integral J or the Rice method [23] is postulated through the equation

$$J = \oint \left(W_e(\varepsilon) n_i - \sigma_{ij} n_j \frac{\partial u_i}{\partial x} \right) \mathrm{d}s, \tag{28}$$

where W_e is the strain energy density and u represents the separation vector at a point $M(s)$ belonging to the contour that defines the crack.

It could be noted throughout the expression postulated above that the integral J represents the decay rate of the potential energy W_p per unit area, which corresponds to the energy release rate:

$$J = -\frac{\partial W_p}{\partial A} = G. \tag{29}$$

The Rice hypothesis [23] integrates the behaviour of elasto-plastic materials in monotonic tension with that of nonlinear elastic materials. Therefore, in the case of our material, the energy release rate can be written as an integral J, which can be determined numerically by the finite element method.

However, it should be noted that the integral J only allows the total energy release rate G_T^C and does not provide those of each failure mode, G_{I}^C, G_{II}^C and G_{III}^C.

On the other hand, this method aids in the computation of the stress intensity factors K_{I}, K_{II} and K_{III} of the three failure modes. Irwin G. R. [24] took up the work of Griffith A. A. [25], where the energy approach has been reformulated in terms of stresses. Therefore, it is a question of monitoring the propagation of failure by the investigation of both stresses and displacements at the crack tip.

The relationship between the energy release rate and the stress intensity factors established by Irwin is defined as

$$G = \frac{{K_{\mathrm{I}}}^2 + {K_{\mathrm{II}}}^2}{E'} + \frac{{K_{\mathrm{III}}}^2}{2\mu}, \tag{30}$$

where $\mu = E'/2(1+\vartheta)$ and $E' = E$ in the in-plane stress case under study.

Therefore, the relationships between the critical energy release rate and the stress intensity factor according to each failure mode are postulated by the following expressions:

$$G_{\mathrm{I}}^C = \frac{K_{\mathrm{IC}}^2}{E'}; \quad G_{\mathrm{II}}^C = \frac{K_{\mathrm{IIC}}^2}{E'}; \quad G_{\mathrm{III}}^C = \frac{K_{\mathrm{III}}^2}{2\mu}. \tag{31}$$

Results:

In the following section, the finite element model developed to determine the stress intensity factors as well as the integral J is presented. A cracked ±55° longitudinal specimen has been modelled (Figure 12(a)). The linear brick element "C3D8R" has been used. The mesh has been refined at the crack tip (Figure 12(b)). Regarding the boundary conditions, one extremity has been fixed and the other has been loaded at a constant displacement of 5 mm. Only the area between the jaws has been considered.

A static stress analysis has been performed via Abaqus with the option of calculating the integral J of the defined crack. Table 5 provides the release energy rate values deduced from the stress intensity factors by using the relationships presented above.

4.3. *Finite element model*

The theoretical model presented and identified above has been implemented in the Abaqus finite element software. In fact, the tensile behaviour of ±55° longitudinal representative specimens has been simulated and observed with the aim of evaluating the performance of the model.

These tests have been accompanied by strain measurements using classical methods that provide information, allowing a comparison with numerical analysis. The choice of semi-structures

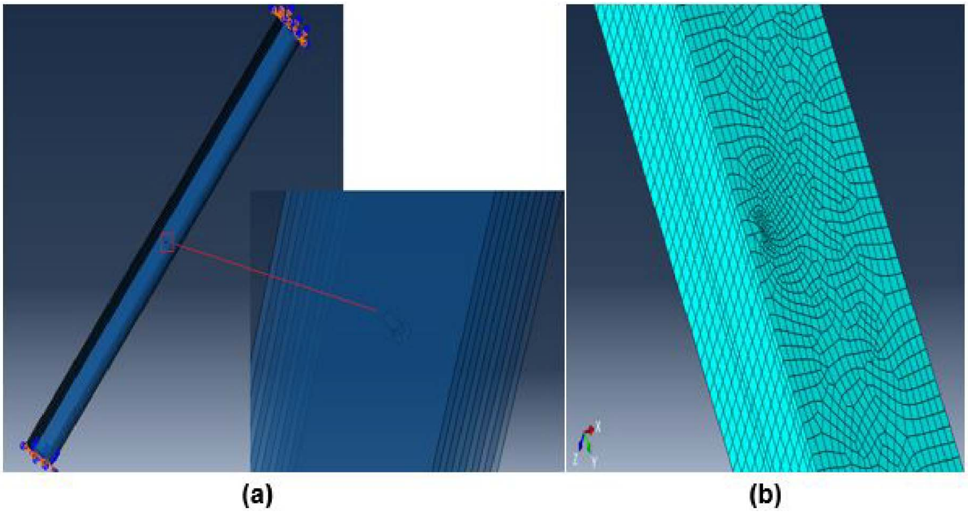

Figure 12. Crack modelling: (a) crack location; (b) mesh view.

(specimens cut from tubes) for the validation of the numerical model has been based on the fact that carrying out experimental tests on a whole tube is difficult, laborious and expensive. Thus, it appeared appropriate to use representative specimens able to capture the phenomena appearing in the tubes during their loading.

Therefore, the same experimental set-up in the model identification has been used in its validation.

The numerical model developed to simulate inter-laminar and intra-laminar damages appearing in the representative specimen loaded is a 3D meso-scale finite element model. The whole laminate has been divided into 10 sections (plies) of 0.5 mm thickness each, separated by cohesive layers of zero thickness. The plies have been discretized using an eight-node integration element (SC8R) called the "continuum shell".

Regarding the cohesive layers, they have been modelled using an eight-node cohesive element called COH3D8 [26].

Two different types of materials have been included according to the two constituents of the structure. The material of the cohesive layers has been defined directly on the CAE Abaqus interface thanks to the material definition module already integrated in its library. However, the definition of the ply material has required the "user definition" module. The computational algorithm describing the ply behaviour has been written and implemented in the Abaqus code through the UMAT subroutine.

An assembly of 10 plies and 9 cohesive layers across the thickness defines the complete model. This assembly has been constructed in such a way so as to maintain continuity between plies before the damage occurs. In fact, a connection has been made between the cohesive layers and the plies using the boundary condition "tie".

To evaluate the performance of the model, tensile behaviours of ±55° longitudinal specimens have been simulated (Figure 13) and observed.

It should be noted that in the simulation of the longitudinal specimens, the curvature has been neglected and only the area between the jaws has been modelled. Regarding the boundary conditions, one side has been fixed to represent the grip of the jaws and a displacement has been imposed on the opposite side.

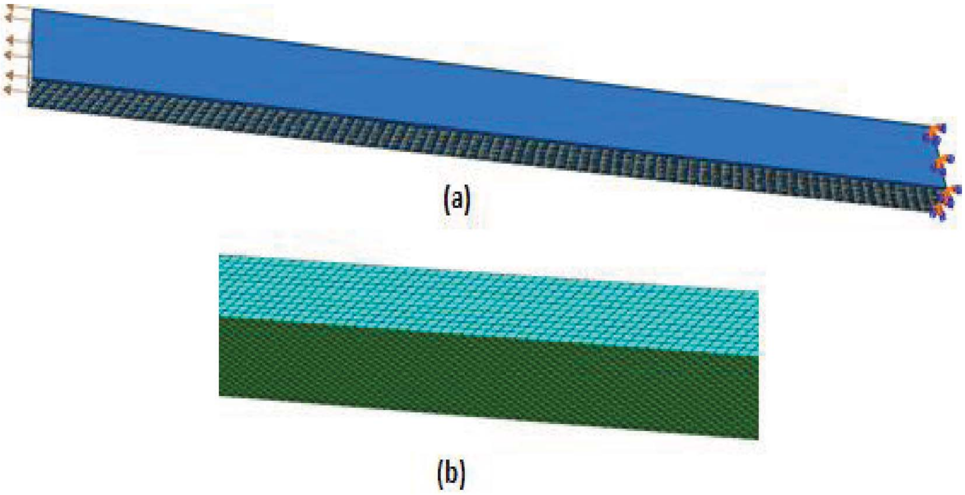

Figure 13. Numerical simulation of ±55° longitudinal specimen loaded in tension: (a) boundary conditions; (b) view of mesh.

5. Experimental validation of the model

5.1. *Methodology*

Experimental validation of the numerical model has been carried out for longitudinal specimens. The strain measurement technique has been employed using strain gauges, and only one type of test has been performed, which is the tensile test.

5.2. *Results and discussions*

Figure 14 illustrates a comparison between the experimental tensile behaviour of a longitudinal specimen and its corresponding simulation. A good agreement between the experimental and numerical results can be noted. This confirms the good level of efficiency of the numerical model developed to simulate the tension behaviour of longitudinal specimens cut from ±55° glass/polyester tubes.

6. Conclusions and perspectives

The ultimate goal of the work presented in this paper is to develop a simple yet effective numerical model allowing the simulation of complex behaviour of filament wound composite structures.

Based on a detailed theoretical study of the material behaviour developed in a previous work, a numerical model has been established.

The identification of this model was of major interest to this study. Several experimental tests have been carried out to identify the different parameters of the damage model.

However, the experimental determination of transverse shear properties was impossible. To estimate their values, a theoretical method has been used, which could affect the reliability of the model developed. Overcoming this limitation by finding the most exact model parameters is therefore one of the aims of this work, which is always considered a major challenge because of its difficulty.

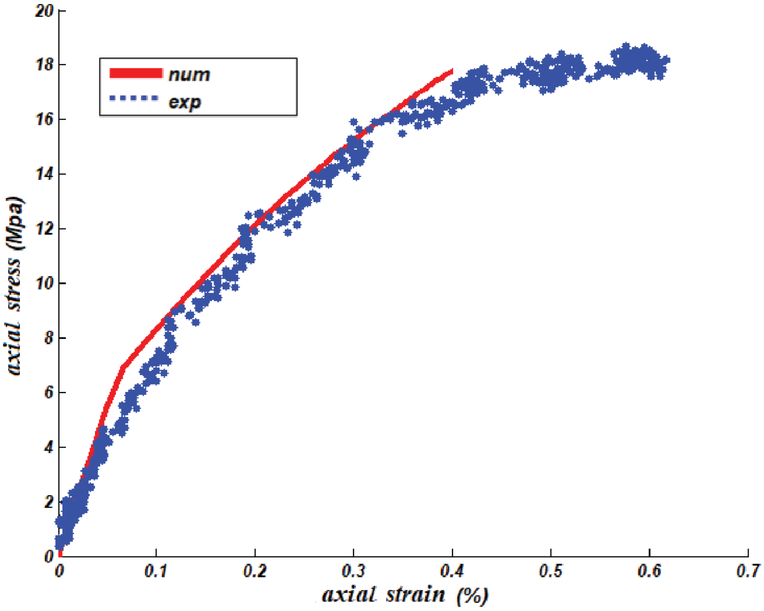

Figure 14. Experimental tensile behaviour of ±55° longitudinal specimen and its corresponding simulation.

In this study, through the development of a 3D meso-scale numerical model and based on "continuum damage mechanics", it was possible to simulate the initiation as well as the progression of all damage phenomena that may occur under loading in the material under study.

The efficiency of the model developed in this study has been assessed by a set of experimental tests.

Numerical simulations of representative specimens loaded with tension have been developed and then compared with the corresponding experimental observations.

Results close to the experimental values have been obtained, which ensures a good level of reliability of the numerical model developed in this study. This might pave the way for the use of this model in industrial applications. In addition, a simulation of more complex structures obtained by filament winding will be the subject of upcoming work.

References

[1] F. Shen, "A filament-wound structure technology overview", *Mater. Chem. Phys.* **42** (1995), p. 96-100.

[2] P. Laney, "*Use of Composite Pipe Materials in the Transportation of Natural Gas*", Idaho National Engineering and Environmental Laboratory, Bechtel BWXT Idaho, LLC (2002).

[3] M. Mohitpour, H. Golshan, A. Murray, "*Pipeline Design & Construction: A Practical Approach, Third Edition*" ASME order number 802574, New York, 2007.

[4] V. G. Tsyss, S. M. Yu, "Simulating of the composite cylindrical shell of the pipe of the supply pipelines based on ANSYS package", *Proc. Eng.* **152** (2016), p. 332-338.

[5] V. Gunasegaran, R. Prashanth, M. Narayanan, "Experimental investigation and finite element analysis of filament wound GRP pipes for underground applications", *Proc. Eng.* **64** (2013), p. 1293-1301.

[6] S. Sulaiman, S. Borazjani, S. H. Tang, "Finite element analysis of filament-wound composite pressure vessel under internal pressure", *IOP Conf. Ser. Mater. Sci. Eng.* **50** (2013), article no. 012061.

[7] I. Vasović, *Strength Analysis of Filament-wound Composite Tubes*, Hemijska industrija, 2010.

[8] R. Roham, A. Ali., "Modeling and experimental evaluation of functional failure pressures in glass fiber reinforced polyester pipes", *Comput. Mater. Sci.* **96** (2015), p. 579-588.

[9] P. F. Liu, L. J. Xing, Y. Zheng, "Failure analysis of carbon fiber/epoxy composite cylindrical laminates using explicit finite element method", *Compos. Part B* **56** (2014), p. 54-61.

[10] P. F. Liu, J. K. Chu, S. J. Hou, J. Y. Zheng, "Numerical simulation and optimal design for composite high-pressure hydrogen storage vessel: a review", *Renew. Sustain. Energy Rev.* **16** (2012), no. 4, p. 1817-1827.

[11] H. Boussetta, M. Beyaoui, A. Laksimi, L. Walha, M. Haddar, "Study of the filament wound glass/polyester composite damage behaviour by acoustic emission data unsupervised learning", *Appl. Acoust.* **127** (2017), p. 175-183.

[12] ISO, "*Plastics Piping Systems – Glass-Reinforced Thermosetting Plastics (GRP) Pipes – Test Methods for the Determination of the Initial Longitudinal Tensile Strength*, published in ISO Standards, no ISO 8513, 2016".

[13] ASTM, "*Standard Test Method for Apparent Hoop Tensile Strength of Plastic or Reinforced Plastic Pipe*, published in ASTM Standards series, no D2290".

[14] E. J. Barbero, P. Lonetti, "An inelastic damage model for fiber reinforced laminates", *J. Compos. Mater.* **36** (2002), no. 8, p. 941-962.

[15] L. M. Kachanov, "On time to rupture in creep conditions (in russian)", *Izv. Akad. Nauk SSSR, Otdelenie Tekhnicheskikh Nauk* **8** (1958), p. 26-31.

[16] Y. N. Rabotnov, "Creep Rupture", in *Applied Mechanics* (M. Hetenyi, H. Vincenti, eds.), Stanford University, 1968, p. 342-349.

[17] S. W. Tsai, E. M. Wu, "A general theory of strength for anisotropic materials", *J. Compos. Mater.* **5** (1971), p. 58-80.

[18] C. L. Tsai, I. M. Daniel, "Determination of in-plane and out-of-plane shear moduli of composite materials", *Exp. Mech.* **30** (1990), no. 3, p. 295-299.

[19] S. Sridharan, *Delamination Behaviour of Composites*, Woodhead Publishing, 2008.

[20] G. I. Barenblatt, "The mathematical theory of equilibrium cracks in brittle fracture", *Adv. Appl. Mech.* **7** (1962), p. 55-129.

[21] Abaqus, Analysis User's Manual version 6.12; "Defining the constitutive response of cohesive elements using a traction-separation description" section 32.5.6, , ABAQUS, Inc. 2012.

[22] M. Benzeggagh, M. Kenane, "Measurement of mixed-mode delamination fracture toughness of unidirectional glass/epoxy composites with mixed-mode bending apparatus", *Compos. Sci. Technol.* **56** (1996), p. 439-449.

[23] J. R. Rice, "Plane strain deformation near a crack tip in a power-law hardening material", *J. Mech. Phys. Sol.* **16** (1968), p. 1-12.

[24] G. R. Irwin, "Fracture", in *Handbuch der Physik* (S. Flügge, ed.), vol. 6, Springer, Berlin, 1957, p. 551-590.

[25] A. A. Griffith, "The phenomena of rupture and flow in solids", *Phil. Trans. R. Soc. Lond. A* **221** (1921), p. 163-198.

[26] Abaqus, *Analysis User's Manual Volume V: Prescribed Conditions, Constraints & Interactions,*version 6.12, ABAQUS, Inc. 2012.